JOURNAL OF AIRCRAFT
Vol. 45, No. 6, November–December 2008

Check for updates

Nonlinear Stability Analysis of Control Surface Flutter with Free-Play Effects

James T. Gordon,* Edward E. Meyer,† and Robert L. Minogue‡
The Boeing Company, Seattle, Washington 98124-2207

DOI: 10.2514/1.31901

Results are presented from nonlinear stability analyses of control surface flutter that were conducted on a three-degree-of-freedom typical-section airfoil with free play about the control surface hinge line. The describing function (harmonic-balance) method has been used to predict response amplitudes, and a locally parameterized continuation method has been used to track all flutter modes. The methodology is directly applicable to systems with unsteady air loads expressed in either the frequency or time domains. Both stable and unstable limit cycles have been identified. Limit cycle stability has been assessed by examining the change in growth rate due to amplitude perturbations at a given velocity. Limit cycle amplitudes predicted by the describing function method, with frequency-domain unsteady aerodynamics, are shown to compare very well with the magnitudes of time-history responses obtained by direct integration of the equations of motion, using rational function approximation time-domain aerodynamics. Results from these nonlinear analyses are compared with analytical and experimental results of similar analyses from the open literature.

Downloaded by UNIVERSITY OF WASHINGTON on August 12, 2019 | http://arc.aiaa.org | DOI: 10.2514/1.31901

Nomenclature

A	=	response amplitude
F_{fp}	=	structural moment about control surface hinge line
F_{δ}	=	describing function for free play nonlinearity
$\hat{F}_{\mathrm{fp}}$	=	nonlinear function of control surface free play
$\hat{\mathbf{F}}_{\mathbf{k}}$	=	vector of nonlinear stiffness terms including free play effects
g	=	growth rate, $g = 2\sigma/\omega$
h	=	typical-section plunge
$\mathbf{K}$	=	stiffness matrix
K_{β}	=	torsional stiffness about control surface hinge line
$K_{\beta\mathrm{eq}}$	=	equivalent stiffness about control surface hinge line
$\mathbf{M}$	=	mass matrix
p	=	complex reduced frequency, $p = s/v_t$
$\mathbf{Q}_{\mathbf{k}}$	=	unsteady aerodynamic matrix
$\mathbf{q}$	=	vector of state variables
q_k	=	kth coordinate in state vector $\mathbf{q}$
$\mathbf{q}_{\mathbf{nl}}$	=	nonlinear vector of coordinate amplitudes
s	=	Laplace variable
t	=	independent variable time
$\mathbf{u}$	=	flutter eigenvector
$\hat{\mathbf{u}}$	=	renormalized flutter eigenvector for β_s
u_j	=	jth coordinate of $\mathbf{u}$
$u_{\beta R}$, $u_{\beta I}$	=	real and imaginary parts of u_{β}
U	=	system parameter (flow speed)
U_f	=	flutter speed
U_0	=	critical value of U
α	=	typical-section pitch
β	=	control surface rotation
β_s	=	control surface rotation amplitude
δ_{fp}	=	rotational free play about control surface hinge line
λ	=	eigenvalue, $\lambda = \sigma \pm j\omega$
τ_{β}	=	structural torque about hinge line
$\mathbf{\Phi}$	=	mode matrix
ϕ, $\bar{\phi}$	=	phase angles
ω	=	frequency, dependent on amplitude A
ω_0, ω_f	=	flutter frequencies for U_0 and U_f

Received 20 August 2007; revision received 31 March 2008; accepted for publication 10 April 2008. Copyright © 2008 by the American Institute of Aeronautics and Astronautics, Inc. All rights reserved. Copies of this paper may be made for personal or internal use, on condition that the copier pay the $10.00 per-copy fee to the Copyright Clearance Center, Inc., 222 Rosewood Drive, Danvers, MA 01923; include the code 0021-8669/08 $10.00 in correspondence with the CCC.

*Associate Technical Fellow, Commercial Airplanes, Flutter Methods, P.O. Box 3707 Mail Code 03-KR. Associate Fellow AIAA.

†Associate Technical Fellow, Commercial Airplanes, Flutter Methods, P.O. Box 3707 Mail Code 03-KR.

‡Structural Analysis Engineer, Commercial Airplanes, 747 Dynamic Loads and Flutter Engineering, P.O. Box 3707 Mail Code 03-KR.

I. Introduction

THE need to include nonlinearities in aeroelastic analyses for the accurate prediction of system stability characteristics is well known, and considerable effort has been devoted to understanding this problem area, experimentally and analytically, during the last five decades. Recent survey papers by Dowell and Tang [1] and Dowell et al. [2] provide comprehensive reviews of current state-of-the-art practices in nonlinear aeroelasticity. In general, the nonlinearities arise from either structural or aerodynamic sources. Typical structural examples are nonlinearities due to stiffness (e.g., free play, hysteresis, geometric hardening or softening) and damping (e.g., Coulomb friction). Typical aerodynamic examples are nonlinearities due to large shock motion or flow separation.

Over the past decade, significant efforts have been made to improve the understanding of nonlinear aerodynamic phenomenon and develop analytical or numerical techniques for predicting the unsteady forces and moments. Computational fluid dynamics (CFD) codes used have included transonic nonlinear potential flow theory (with and without viscous effects) in addition to Euler-based and Navier–Stokes flow models (Dowell et al. [2] and Schuster et al. [3]). However, as noted by Dowell et al. [2], standard CFD codes are too expensive or time-consuming to use for most aeroelastic analyses now and for the foreseeable future. Yurkovich [4] notes that CFD generally has not made a significant contribution to production flutter analyses and offers the opinion that the doublet-lattice method will continue to be the predominant unsteady aerodynamic tool for aeroelastic analyses for a long time.

The Krylov–Bogoliubov [5] (K–B or harmonic balance) and describing function [6] methods have been applied successfully to systems with nonlinearities ranging from single-valued continuous and piecewise continuous functions to relay types with discontinuous jumps (e.g., Coulomb friction, free play, hysteresis). Application of these procedures is justified, even with strong nonlinearities, if the system possesses a filtering property that attenuates responses at the higher harmonic frequencies, that is, the system admits a periodic solution dominated by the fundamental harmonic. Popov [7] has given the conditions that must be satisfied by the system and the nonlinear function for the Krylov–Bogoliubov

Downloaded by UNIVERSITY OF WASHINGTON on August 12, 2019 | http://arc.aiaa.org | DOI: 10.2514/1.31901

averaging method to be applicable. In general, system models for nonlinear flutter problems exhibit this filtering property. The describing function method has been applied successfully to flutter analyses of aircraft for a variety of structural nonlinearities [8–17]. Shen [9] has discussed the suitability and application of the K–B method to nonlinear flutter problems. Šiljak [6] discussed the applicability criterion of Popov [7] in considerable detail for the describing function and Krylov–Bogoliubov methods, including extensions to systems having multiple nonlinearities of symmetric and nonsymmetric types. Šiljak [6] also notes that if the applicability conditions of Popov [7] are not satisfied, use of these methods may predict sustained oscillations that do not exist or may fail to predict sustained oscillations that do exist. Bogoliubov and Mitropolskii [18] have investigated the nonlinear analysis of self-excited systems using harmonic-balance methods. Morrison [19] discussed the close relationship between averaging methods and the two-variable expansion procedure [20,21]. Generalization of the two-variable expansion procedure using multiple time scales and the validity of the asymptotic expansion method were discussed by Nayfeh [22]. Applications of averaging techniques and the multiple-time-scale method to free, forced, and self-excited vibration problems with a variety of nonlinearities, including some with relay characteristics, were given by Nayfeh and Mook [23,24].

Much work has also been done over the past decade investigating the effects of various structural nonlinearities on aeroelastic characteristics. Experimental and analytical studies conducted by Conner et al. [25], Tang et al. [26,27], and Trickey et al. [28] have investigated the nonlinear flutter behavior of a three-degree-of-freedom typical-section airfoil with control surface free play. These analytical studies have used both direct time integration and describing function (harmonic-balance) methods to determine limit cycle amplitudes and have compared predicted responses with experimental data.

Direct time integration of the nonlinear equations of motion can be used to obtain response histories for the control surface flutter problem. This is certainly a major advantage of the direct integration approach (i.e., a response solution can be obtained). However, the major disadvantages with direct integration for determining limit cycle oscillation (LCO) responses include the following:

1) This approach is very costly and time-consuming because there are an infinite number of initial conditions that must be evaluated for each flow speed to search for the existence of limit cycles.

2) This approach cannot assess limit cycle stability issues except by brute force trial and error, which further increases costs and time requirements.

The describing function method can directly obtain both stable and unstable limit cycles, including multiple limit cycles at a single flow speed. A major advantage of the describing function method is its straightforward application, although it still requires considerable computational effort and stability must be determined after the amplitude-vs-airspeed dependence has been determined. The major drawbacks are as follows:

1) Use of the describing function method cannot guarantee that all limit cycles have been found, although this does not seem to be a serious problem in practice.

2) Extension of the analysis to higher orders is considerably more difficult for the describing function method than for more general perturbation methods such as the generalized averaging or multiple-time-scale techniques.

In previous work that used the describing function technique to obtain LCO amplitudes, limit cycles were identified as being stable or unstable, but no detailed explanation has been given about the method used to evaluate LCO stability [9–17,25–27]. Also, the requirement for accurate tracking of all flutter modes both to determine flutter crossings (speed and frequency) at a particular control surface rotational stiffness and to track LCO amplitude and frequency vs flow speed, as the effective rotational stiffness of the control surface is varied, has not been addressed.

The goal of the work presented here was to develop a nonlinear stability analysis of control surface flutter, including free play about the control surface hinge line using the describing function method, that is directly applicable to systems with unsteady air loads expressed in either the frequency or time domains. The analysis obtains limit cycle amplitude and frequency as functions of flow velocity using a locally parameterized continuation method to track all flutter modes. Limit cycle stability is assessed by examining the change in growth rate due to amplitude perturbations at a given flow velocity.

II. Solution Methodology

A. Problem Formulation

The equations of motion for nonlinear flutter models considered here have the general form shown in Eq. (1) when expressed in state variable representation

$$\mathbf{M}\,\dot{\mathbf{q}} + \mathbf{K}\mathbf{q} = \hat{\mathbf{F}}_{\mathbf{k}}(\hat{F}_{\mathrm{fp}}, q_k) \tag{1}$$

$\mathbf{M}$ is a matrix of inertia terms and $\mathbf{K}$ is a matrix containing structural and aerodynamic stiffness and damping terms for the linear system about an equilibrium point $\mathbf{q_e}$ when the equations of motion are expressed in terms of the state variable vector $\mathbf{q} = \{q_1, q_2, \ldots, q_{2N}\}^T$ and $\dot{q}_j = q_{2j}$ for the jth coordinate, where $j = 1, 2, \ldots, N$. A dot over a symbol indicates differentiation with respect to time t.

It is assumed that the unsteady aerodynamic forces and moments in Eq. (1) are either specified in the frequency domain (as functions of reduced frequency) or have been transformed to the time domain using the rational function approximation (RFA) of Roger [29], or an equivalent procedure. For time-domain simulations, the generalized unsteady aerodynamic matrices can be approximated using a least-squares fit of a certain rational polynomial to a set of complex matrices. Given a set of m unsteady aerodynamic matrices $\mathbf{Q_k} = \mathbf{Q}(p_k)$ at various values of the complex reduced frequency $p = s/v_t$, where $k = (1, 2, \ldots, m)$, s is the Laplace variable and v_t is the true airspeed, the unsteady aerodynamic terms can be approximated with an analytic function of p. The Roger's rational function approximation (RFA) to the aerodynamic matrix Q has the form

$$\mathbf{Q}\,(p) \approx \mathbf{R_0} + p\mathbf{R_1} + p^2\mathbf{R_2} + \sum_{i=1}^{l} \frac{p}{p+\beta_i}\mathbf{R_{i+2}} \tag{2}$$

where the matrices $\mathbf{R_i}$ and the aerodynamic lag poles β_i are real. The least-squares solution is accomplished by specifying the β_i and determining the coefficient matrices $\mathbf{R_i}$ to approximate the aerodynamic matrix $\mathbf{Q}(p)$.

The vector $\hat{\mathbf{F}}_k = \hat{\mathbf{F}}_k(\hat{F}_{\mathrm{fp}}, q_k)$ in Eq. (1) is a nonlinear function of q_k representing terms due to structural free play in the linkages about the control surface hinge line. The structural moment F_{fp} about the control surface hinge line, including free-play effects, is given by

$$F_{\mathrm{fp}} = K_\beta q_k + \hat{F}_{\mathrm{fp}} \tag{3}$$

where

$$\hat{F}_{\mathrm{fp}} = \begin{cases} -K_\beta \delta_{\mathrm{fp}}, & q_k > +\delta_{\mathrm{fp}} \\ -K_\beta q_k, & |q_k| \le +\delta_{\mathrm{fp}} \\ +K_\beta \delta_{\mathrm{fp}}, & q_k < -\delta_{\mathrm{fp}} \end{cases} \tag{4}$$

so that

$$F_{\mathrm{fp}} = \begin{cases} K_\beta (q_k - \delta_{\mathrm{fp}}), & q_k > +\delta_{\mathrm{fp}} \\ 0, & |q_k| \le +\delta_{\mathrm{fp}} \\ K_\beta (q_k + \delta_{\mathrm{fp}}), & q_k < -\delta_{\mathrm{fp}} \end{cases} \tag{5}$$

K_β is the torsional stiffness of the control surface about its hinge line. $\hat{F}_{\mathrm{fp}}$, which is given by Eq. (4), is a function of q_k and the free play δ_{fp}. The linear term $K_\beta q_k$ in F_{fp} (which is assumed to be a function of $q_k = \beta$ here for simplicity only) is included in $\mathbf{K}$.

Let U be a system parameter that is the fluid flow speed. There is a critical value $U = U_0$ such that the linear system ($\hat{\mathbf{F}}_{\mathbf{k}} = \mathbf{0}$) is stable for $U < U_0$ and unstable for $U > U_0$. For $U = U_0$, there is one pair of

Downloaded by UNIVERSITY OF WASHINGTON on August 12, 2019 | http://arc.aiaa.org | DOI: 10.2514/1.31901

purely imaginary eigenvalues; all other eigenvalues have negative real parts. Thus, undamped harmonic oscillations occur for $U = U_0$. The periodic solution of Eq. (1) is sought in the local neighborhood of U_0 for small perturbations about the equilibrium point $\mathbf{q_e} = \mathbf{0}$. The vibration amplitudes are assumed to be high enough to exceed the control surface free-play dead zone, that is, $q_k \geq \delta_{\text{fp}}$.

B. Describing Function Method

The fundamental assumption of the describing function method [6] is that given a sinusoidal input the only significant output of a nonlinear element is a sinusoidal component at the input frequency. It is assumed that higher harmonics do not significantly affect the system's behavior. No additional restrictions are made for other signals in the system.

Application of the describing function method is equivalent to computing the Fourier components for the nonlinearity, retaining only the first-order term, and, thus, generating an equivalent linear system. For a symmetric free-play nonlinearity with no preload, the restoring torque τ_β about the control surface hinge line is given by

$$\tau_\beta = \begin{cases} K_\beta(\beta - \delta_{\text{fp}}), & \beta > +\delta_{\text{fp}} \\ 0, & |\beta| \leq +\delta_{\text{fp}} \\ K_\beta(\beta + \delta_{\text{fp}}), & \beta < -\delta_{\text{fp}} \end{cases} \tag{6}$$

where K_β is the stiffness coefficient outside the free-play region, β is the rigid rotation about the control surface hinge line, and $2\delta_{\text{fp}}$ is the total free play.

Assuming a fundamental harmonic solution for the control surface rotation β of the nonlinear system, where $\beta = \beta_s \sin(\omega t)$, application of the describing function technique [6] to the expression for τ_β given in Eq. (6) determines an equivalent rotational stiffness $K_{\beta\text{eq}}$.

$$K_{\beta\text{eq}} = F_\delta K_\beta \tag{7}$$

In Eq. (7), F_δ is the describing function for the free-play nonlinearity and is a function of control surface rotation amplitude β_s and free play δ_{fp}, as given in Eqs. (8) and (9). F_δ is a transcendental function of the variable $T = \sin^{-1}(\delta_{\text{fp}}/\beta_s)$ that is nonlinear and single-valued as shown in Fig. 1. For zero free play, that is, $\delta_{\text{fp}} = 0$, note that $F_\delta = 1$ and $K_{\beta\text{eq}} = K_\beta$:

$$F_\delta = \begin{cases} 0, & -\delta_{\text{fp}} < \beta_s < +\delta_{\text{fp}} \\ 1 - \frac{2}{\pi}[T + \sin T \cos T], & +\delta_{\text{fp}} \leq |\beta_s| \end{cases} \tag{8}$$

$$T = \sin^{-1}(\delta_{\text{fp}}/\beta_s) \tag{9}$$

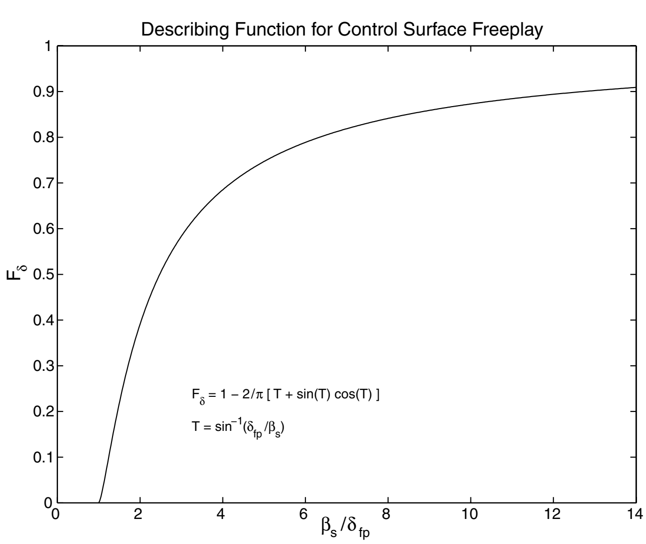

Fig. 1 Describing function for free-play nonlinearity.

If the nonlinear term τ_β, defined in Eq. (6), or F_{fp}, in Eq. (5), is replaced by $K_{\beta\text{eq}}\beta$ in the equations of motion (1), then equivalent linearized equations are obtained. By specifying a value of $K_{\beta\text{eq}}$ and solving the linearized equations, the flutter velocity U_f and the flutter frequency ω_f can be determined as a function of the parameter $K_{\beta\text{eq}}$. Thus, U_f and ω_f are known as functions of the control surface rotational amplitude $\beta = \beta_s$ for a given δ_{fp}. Because β is now known, the amplitudes of all other coordinates (degrees of freedom) can be obtained using the harmonic-balance method. This procedure is summarized as follows:

1) Specify $K_{\beta\text{eq}}$ and δ_{fp}.
2) Linearize the equations of motion (1) by setting $F_{\text{fp}} = K_{\beta\text{eq}}\beta$.
3) Root the linearized system to obtain U_f and ω_f as functions of $K_{\beta\text{eq}}$.
4) Knowing $K_{\beta\text{eq}}$, determine $F_\delta = K_{\beta\text{eq}}/K_\beta$.
5) Determine $\beta_s/\delta_{\text{fp}}$ from Eqs. (8) and (9) for F_δ shown in Fig. 1.
6) For $K_{\beta\text{eq}}$, U_f, ω_f, and β_s, solve the system of linearized equations.
7) Vary $K_{\beta\text{eq}}$.
8) Repeat steps (2–7) to obtain the nonlinear response amplitudes versus U_f.

To determine limit cycle amplitudes, rather than transforming the equations of motion to the time domain and formally applying the harmonic-balance technique, the nonlinear amplitudes can be obtained directly by a rotation and renormalization of the flutter eigenvector. Note that this approach is valid for solutions with either frequency- or time-domain flutter equation formulations.

Assume that the flutter frequency ω_f, speed U_f, and eigenvector $\mathbf{u}$ have been determined for a specific $K_{\beta\text{eqv}} = F_\delta K_{\beta\text{nom}}$ where F_δ is the describing function for a given control surface rotational free play δ_{fp} and rotational amplitude β_s. $K_{\beta\text{nom}}$ and $K_{\beta\text{eqv}}$ are the nominal and equivalent rotational stiffnesses of the control surface, respectively. u_β is the β component of the flutter eigenvector $\mathbf{u}$, and its magnitude R_β is given by $R_\beta^2 = u_{\beta_R}^2 + u_{\beta_I}^2$.

Because the flutter eigenvector is being rotated and renormalized to obtain the nonlinear amplitudes corresponding to the beta coordinate value β_s, the component u_β must be scaled by (β_s/R_β) and rotated by $\bar{\phi} = -(\frac{\pi}{2} + \phi)$ where $\phi = \tan^{-1}(u_{\beta_I}/u_{\beta_R})$ to yield $\hat{u}_\beta = -i\beta_s$ (where $\hat{\mathbf{u}}$ is the rotated and renormalized eigenvector) so that $q_\beta = \beta = \beta_s \sin \omega t$ as required.

Hence, the complex amplitudes for all coordinates are obtained by scaling and rotating the flutter eigenvector $\mathbf{u}$ by the same factor (β_s/R_β) and angle $\bar{\phi}$, respectively. Thus, the complex amplitudes for all coordinates are given by

$$\hat{\mathbf{u}} = \mathbf{u} e^{i\bar{\phi}} \beta_s / [u_{\beta_R}^2 + u_{\beta_I}^2]^{1/2} \tag{10}$$

where $\bar{\phi} = -(\pi/2 + \phi)$ and $\phi = \tan^{-1}(u_{\beta_I}/u_{\beta_R})$. The nonlinear amplitude of each coordinate is given by the magnitude of its complex component of $\hat{\mathbf{u}}$

$$|\hat{u}_j| = [\hat{u}_{jR}^2 + \hat{u}_{jI}^2]^{1/2} \tag{11}$$

C. Limit Cycle Stability Criteria

Popov [7] investigated the relative stability of periodic oscillations by evaluating the effects of small amplitude variations on the imaginary roots of the characteristic equation of the linearized system (obtained by using only the first approximation in linearizing the nonlinear system). Evaluation of limit cycle stability by this approach is given by Šiljak [6]. It is shown that the stability of sustained oscillations may be transferred into the algebraic domain (i.e., the s-plane) and solved by a sensitivity analysis of the characteristic roots of the system equations.

Assume that for some frequency $\omega \neq 0$ and amplitude A, the system has a pure imaginary root and all the other $n - 1$ roots lie in the left half of the s-plane. Assume that the eigenvalue is $\lambda = \sigma \pm j\omega$, where σ is the real part of the eigenvalue λ, j is the imaginary unit $\sqrt{-1}$, and ω is the frequency. At the flutter point, and

Downloaded by UNIVERSITY OF WASHINGTON on August 12, 2019 | http://arc.aiaa.org | DOI: 10.2514/1.31901

for a limit cycle, $\sigma = 0$ for $A = A_{\mathrm{LC}}$. Here, for the nonlinear system, the damping term is a function of the amplitude, that is, $\sigma = \sigma(A)$.

Stability of the periodic solution ($\sigma = 0$) is determined by the change in amplitude A when $\sigma = 0$. If, for an increase in the amplitude A from its value A_{LC} for the periodic solution (i.e., at the limit cycle), the function $\sigma(A)$ changes sign from $+$ to $-$, the periodic solution is stable and vice versa. Hence, stability of the periodic solution is determined by the sign of the ratio $\Delta\sigma/\Delta A$ rather than merely the sign of $\sigma(A)$. The stability analysis by Šiljak [6] obtains the following criteria for the existence of sustained oscillations.

For a stable limit cycle to exist, the following condition must hold:

$$\left\{\frac{\partial\sigma}{\partial A}\right\}_{A=A_{\mathrm{LC}}} < 0 \tag{12}$$

For an unstable limit cycle to exist, the following condition must hold:

$$\left\{\frac{\partial\sigma}{\partial A}\right\}_{A=A_{\mathrm{LC}}} > 0 \tag{13}$$

For a semistable limit cycle that is stable at small amplitudes and unstable at large amplitudes to exist, the following two conditions must hold:

$$\left\{\frac{\partial\sigma}{\partial A}\right\}_{A=A_{\mathrm{LC}}} = 0 \tag{14}$$

and

$$\left\{\frac{\partial^2\sigma}{\partial A^2}\right\}_{A=A_{\mathrm{LC}}} > 0 \tag{15}$$

For a semistable limit cycle that is stable at large amplitudes and unstable at small amplitudes to exist, the following two conditions must hold:

$$\left\{\frac{\partial\sigma}{\partial A}\right\}_{A=A_{\mathrm{LC}}} = 0 \tag{16}$$

and

$$\left\{\frac{\partial^2\sigma}{\partial A^2}\right\}_{A=A_{\mathrm{LC}}} < 0 \tag{17}$$

These limit cycle stability criteria are depicted in Fig. 2.

D. Implementation Using Continuation Methodology

The describing function methodology outlined previously has been incorporated into The Boeing Company's proprietary program Apex to allow nonlinear response calculations of control surface flutter with free-play effects. Displacement, velocity, and acceleration responses for any nodal location or nodal degree of freedom can be obtained as functions of flow speed and free play (i.e., dead-zone magnitude or gap size).

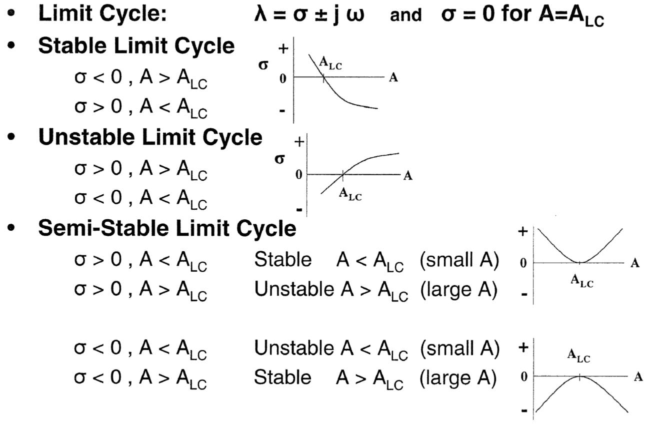

Fig. 2 Limit-cycle stability criteria.

Apex is a package of programs used at Boeing to perform various dynamics analyses including vibration, dynamic response, linear or nonlinear flutter, and shimmy analyses. In addition to basic stability and response analyses, parameter studies can be conducted using numerous matrix parameterizations. Apex has no structural-model-building capability. Structural finite-element models must be developed either in ATLAS (a Boeing proprietary structural/aeroelastic code), CATIA-ELFINI, or NASTRAN and then imported into Apex. Flutter solutions can be obtained using either the traditional *k method*, the *p method*, or the *p–k method*.

For the flutter models considered here, linear stability is determined by computing roots of the homogeneous characteristic equation

$$\mathbf{D}\mathbf{u} = [s^2\mathbf{M} + (1 + id)\mathbf{K} - q\mathbf{Q}(p, M)]\mathbf{u} = \mathbf{0} \tag{18}$$

where $\mathbf{D}$ is the dynamic matrix, $\mathbf{M}$, $\mathbf{K}$, and $\mathbf{Q}$ are matrices representing inertia, structural stiffness, and unsteady aerodynamic terms, respectively, d is the structural damping term (if present), q is the dynamic pressure, p is the complex reduced frequency, M is the Mach number, and $\mathbf{u}$ is a vector of unknown generalized coordinates. A root or eigenpair of this equation is a pair (s, $\mathbf{u}$), which satisfies Eq. (18). A variety of scalar quantities may or may not appear explicitly in this equation, for example, true airspeed appears only in the definition of dynamic pressure, reduced frequency, and Mach number. Also, user-defined parameters do not appear explicitly, and any of the matrices may be functions of standard and user-defined parameters. A solution to Eq. (18) requires that the dynamic matrix $\mathbf{D}$ is singular, meaning the determinant is zero.

Equation (18) is a system of algebraic equations linear in the generalized coordinates and nonlinear in most other quantities (either explicit or implicit parameters). From this set of n complex equations, an equivalent set of $2n$ real equations can be derived by considering the real and imaginary parts of the residual vector $\mathbf{r} = \mathbf{D}\mathbf{u}$ as separate real variables. Because Eq. (18) is homogeneous in the generalized coordinates, it is necessary to add a constraint to eliminate the trivial solution $\mathbf{u} = \mathbf{0}$. Here, a normalization condition is added as shown in Eq. (19), where $\mathbf{u}^*$ is the complex conjugate of $\mathbf{u}$ and u_k is the component of $\mathbf{u}$ with the largest magnitude

$$\mathbf{u}^*\mathbf{u} = 1 \qquad \Im(u_k) = 0 \tag{19}$$

The resulting set of $2n + 2$ nonlinear real equations to be solved are

$$\mathbf{f}(\mathbf{x}) = \begin{Bmatrix} \Re(r_1) \\ \Im(r_1) \\ \vdots \\ \Re(r_n) \\ \Im(r_n) \\ \mathbf{u}^*\mathbf{u} - 1 \\ \Im(u_k) \end{Bmatrix} \tag{20}$$

where $\Re$ and $\Im$ indicate the real and imaginary parts of the components of the residual vector $\mathbf{r}$, respectively; $\mathbf{f}$ is a real vector of length $2n + 2$; and $\mathbf{x}$ is a vector comprising active parameters and the real and imaginary parts of the components of $\mathbf{u}$. The number of elements in $\mathbf{x}$ is $2n$ (real and imaginary parts of the components of $\mathbf{u}$) plus the number of active parameters. The number of active parameters determines the nature of the solution. Two active parameters yields a point because $2n + 2$ equations in $2n + 2$ unknowns has a unique solution; three active parameters gives a curve; and, four active parameter produces a surface.

Equation (20), with the dimension of $\mathbf{x}$ greater than the dimension of $\mathbf{f}$, can be solved using a continuation method. A continuation method works much like a predictor–corrector solver for ordinary differential equations. Starting from a known solution and using derivatives of the independent variables, a new solution at new

Downloaded by UNIVERSITY OF WASHINGTON on August 12, 2019 | http://arc.aiaa.org | DOI: 10.2514/1.31901

values of the independent variables is predicted. Then, the new solution is obtained using a correction scheme such as Newton's method.

The stability solution module in Apex uses a modified version of a general-purpose package called PITCON [30,31] for solving continuation problems that have one more independent variable than dependent variables. Here, the code solves the problem where the number of unknowns is three greater than the number of generalized coordinates in the flutter equations. Details of the solution method are given by Meyer [32].

Implementation of the describing function method using the continuation procedure is slightly different than that outlined in the preceding paragraphs because the order of certain calculations is switched to fully use the parameterization capability and efficient database structure inherent in the Apex program. The flutter boundary is determined efficiently by tracking the variations in flutter speed and frequency with control surface rotational amplitude β_s and free play δ_{fp} directly in a continuous fashion. In addition, continuity of the flutter boundary itself is an important and useful feature of the solution method.

To trace the flutter boundary, the flutter equations are treated as a system of nonlinear equations parameterized by flutter speed, frequency, control surface rotational amplitude, and free play. This technique is used to determine the flutter boundary in two steps. First, several p–k-type flutter solutions are done at particular values of equivalent control surface rotational stiffness $K_{\beta\text{eq}}$ to determine the lowest flutter speed. Then, using a continuation method, the flutter boundary is traced with the flutter speed as a starting point. For either step, the equations comprise a system of $n+1$ complex equations or $2n+2$ real equations. The generalized coordinates comprise n complex unknowns. Taking three additional parameters as unknowns yields an underdetermined system of $2n+2$ equations in $2n+3$ unknowns. The set of solutions to a system of equations with one more unknown than equations is, in general, a curve. If velocity, frequency, and growth rate are the three additional parameters, the solutions are the usual p–k flutter solutions, and the velocity where the growth rate is zero is the critical flutter speed. Starting with a critical flutter speed and taking the parameters as velocity, frequency, and control surface rotation β_s produces the flutter boundary, a curve of velocity as a function of control surface LCO amplitude β_s for a given value of free play δ_{fp}.

To conduct a nonlinear stability analysis in Apex, the stiffness matrix must first be parameterized with respect to the parameters β_s and free play δ_{fp} with both parameters acting on the same generalized coordinate (here, the control surface rigid rotation). Next, a flutter analysis is conducted at the nominal value of the control surface rotational stiffness $K_{\beta\text{eq}}$. Finally, a parameter variation flutter analysis is performed with the parameter $K_{\beta\text{eq}}$ ranging from zero to its nominal value (or, equivalently, by varying β_s for a given free play δ_{fp}).

The describing function procedure with continuation methodology is summarized as follows:

1) Define active parameters β_s and δ_{fp}, control surface rotational amplitude and free play, respectively, for the generalized coordinate that is the control surface rotational degree of freedom β. This defines the equivalent stiffness $K_{\beta\text{eq}}$ in terms of the describing function F_δ and nominal stiffness $K_{\beta\text{nom}}$.

2) Obtain p–k flutter solutions at a few values of $K_{\beta\text{eq}}$ (i.e., values of β_s/δ_{fp}). Result: flutter crossings (U_f, ω_f) for a specified growth rate, $g = 2\sigma/\omega$.

3) Conduct a parameter variation on β_s and δ_{fp}.

a) Using the describing function, where $K_{\beta\text{eq}} = F_\delta K_{\beta\text{nom}}$, compute F_δ from β_s/δ_{fp} and $K_{\beta\text{eq}}$ from F_δ and $K_{\beta\text{nom}}$.

b) Determine the flutter velocity U_f and frequency ω_f vs β_s/δ_{fp}. Result: K_β vs ω_f and K_β vs U_f curves for a specified growth rate, $g = 2\sigma/\omega$.

4) Compute nonlinear responses for specific nodal locations and degrees of freedom.

a) Extract rows from the modes matrix Φ for the degrees of freedom desired.

b) For each point on the $K_{\beta\text{eq}}$ vs U_f curves determine $\mathbf{q}_{\mathbf{nl}}$: Normalize the generalized coordinate vector so that $|\ \beta\ | = \beta_s$.

c) Divide the displacement by δ_{fp}/β_s giving displacement per unit of free play.

d) Calculate displacements, velocities, and acclerations from $\mathbf{x}_{\mathbf{nl}} = \mathbf{\Phi q}_{\mathbf{nl}}$.

5) Plot the nonlinear responses (displacement/velocity/acceleration).

a) as a function of flow speed U_f,

b) as a function of the control surface free play δ_{fp},

c) as a function of specified growth rate level(s).

III. Three-Degree-of Freedom Typical Section

A. Model Description

The three degree-of-freedom (3 DOF) typical-section model analyzed here is the one tested and analyzed by Conner et al. [25], Tang et al. [26,27], and Trickey et al. [28]. The experimental model tested at Duke University represented a two-dimensional NACA 0012 rectangular wing that included two parts, a main wing with a 19 cm chord and 52 cm span, and a flap with a 6.35 cm chord and 52 cm span. The flap was mounted at the trailing edge of the wing. Details of the model's construction and experimental procedures are fully described by Conner [33] and are summarized briefly here. The flap has a rigid rotational degree of freedom relative to the main wing plus an adjustable support mechanism that provides free play in this rigid rotation coordinate. The model was mounted vertically in the wind tunnel to avoid two problems. When the model was mounted horizontally in the tunnel, a high level of Coulomb (dry) friction was present between the flap hinge bearings and the flap hinge shaft. Even a low friction level in the bearing system could be amplified significantly by any misalignment in the shafts at either end. Also, with the model mounted horizontally, incorporation of free play into the flap rigid rotation degree of freedom includes a preload in the restoring torque due to gravitational loading. Mounting the model section vertically eliminated the preload and helped minimize dry friction levels.

Here, a simple three-degree-of-freedom typical-section flutter model with nonlinearity due to torsional free play about the control surface hinge line is analyzed. The model, depicted in Fig. 3, is based on a linear model proposed by Edwards et al. [34] and used by Conner et al. [25], Tang et al. [26], and Trickey et al. [28] in their investigations of nonlinear flutter due to control surface free-play effects.

The system has a moment of inertia I_α about the pitching axis of the section; a moment of inertia I_β about the hinge line of the control surface; a reference mass m_{ref} (mass of wing plus the mass of the flap all per unit span); torsional stiffness K_α about the pitch axis; torsional stiffness K_β about the hinge line; and linear viscous damping terms ζ_α, ζ_β, and ζ_h in the pitch, flap rotation, and plunge degree of freedom, respectively. The model includes a nonlinear term due to the torsional restoring moment about the flap hinge line including the effect of free play in the flap rotation degree of freedom. Definitions and values of model parameters are given in the Appendix. Conner [33] and Trickey [35] present summaries of the equations of motion based on Theodorsen's derivation for the three-degree-of-freedom system [36].

The nodal arrangement for an ATLAS model of the three-degree-of-freedom typical section is shown in Fig. 4. The ATLAS model consists of a very stiff beam between nodes 1, 20, 21, and 2. Node 1 is the attachment node for two springs, one controlling the plunge coordinate and the other controlling the pitch coordinate. The wing mass is located at node 20 and the aileron mass in located at node 19. The input inertias are chosen to yield the correct mass, inertia, and center-of-gravity (CG) location at the CG of the wing flap (at node 21) and about the aileron hinge line, which is located at node 2 to duplicate Conner's model. The ATLAS aerodynamic model uses the center section only, nodes 3, 12, 13, 14, 15, 16, and 11 as shown in Fig. 4. This model replicates Conner's model using the ATLAS database. The ATLAS aerodynamic model here is a two-dimensional incompressible unsteady (Theodorsen) air-load representation.

Downloaded by UNIVERSITY OF WASHINGTON on August 12, 2019 | http://arc.aiaa.org | DOI: 10.2514/1.31901

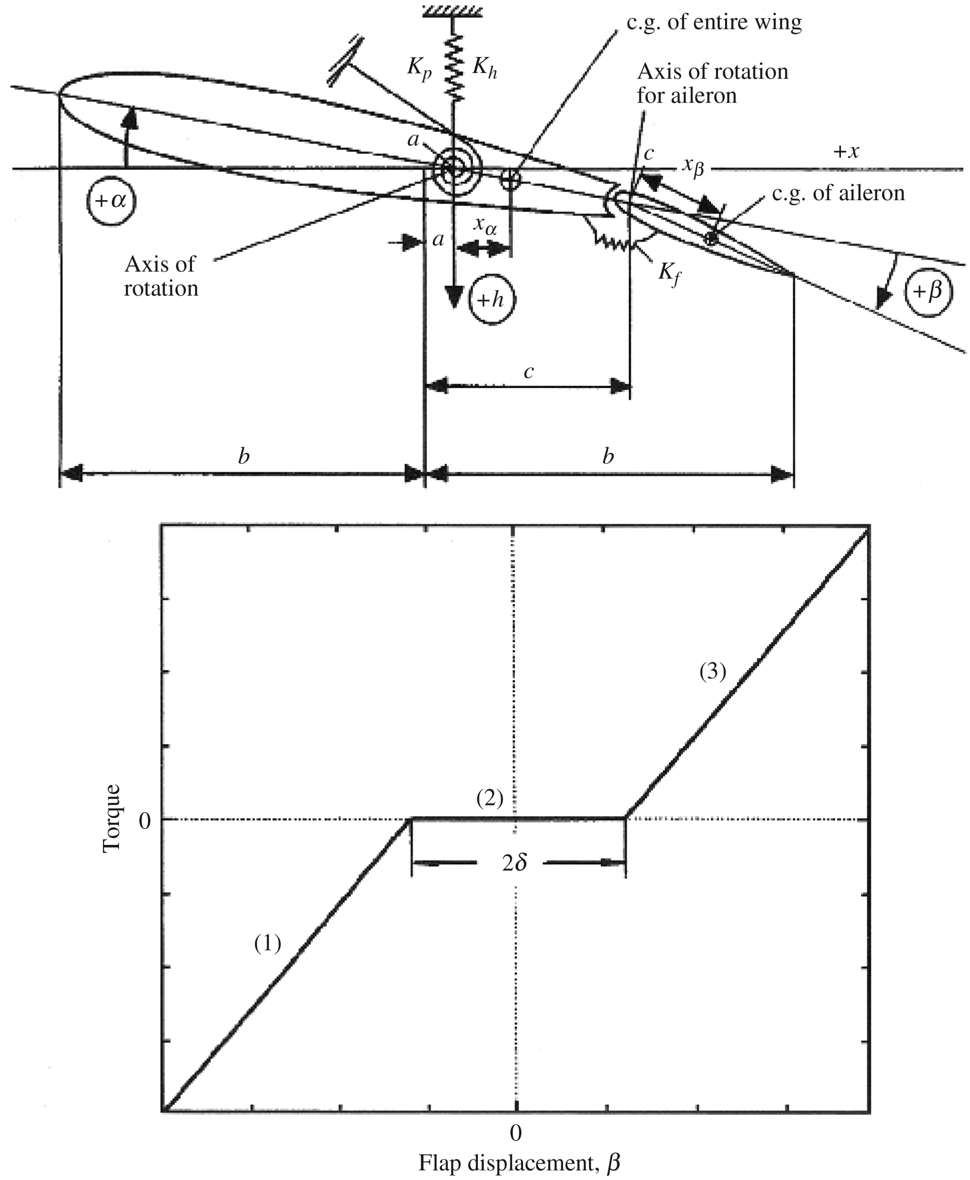

Fig. 3 Three-degree-of-freedom typical-section model.

Unsteady air forces were computed for nine k-values (0.0, 0.005, 0.023, 0.05, 0.1, 0.2, 0.3, 0.5, 0.9), where $k = \omega b_{\mathrm{ref}}/V$ with $b_{\mathrm{ref}} = 1.0$.

As shown by Conner [33], Conner et al. [25], and Tang et al. [26,27], there are four distinct regions of oscillatory behavior for flow speeds less than the flutter speed ($U_f = 23.9$ m/s for Conner's analysis). For velocities $0 < U < 0.18U_f$, any initial disturbance produces oscillations that decay to 0 amplitude fairly quickly (i.e., the system is well damped and stable). At $U \approx 0.18U_f$, there is a discrete jump from the rest state (global steady state) to a low-frequency limit cycle characterized by simple periodic oscillations in the control surface degree of freedom β. The system exhibits the simple low-frequency behavior until a speed $U \approx 0.32U_f$. Here, the system enters a transition region that consists of a more complex periodic low-frequency limit cycle. Several types of nonlinear behavior are present in the transition region including quasi-periodicity. The transition region exhibits increasing amplitudes in all three degrees of freedom as the flow speed increases. At a flow speed $U \approx 0.50U_f$, there is another abrupt change in the system behavior. The low-frequency limit cycle suddenly becomes unstable, and the system is attracted to a stable, high-frequency limit cycle. There is a dramatic drop in the plunge amplitude at this point. The pitch amplitude also drops and then grows again as the flow speed increases whereas the flap amplitude jumps in magnitude and then remains fairly constant. Also, the high-frequency flap motion returns to a simple periodic-type oscillation. Shortly after onset of this high-frequency limit cycle oscillation, the transient oscillations exhibit the character of the quasi-periodic oscillations present in the transition region.

Analytical results obtained by Conner et al. [25] and Trickey et al. [28] used unsteady air loads in the time domain based on Edward's state-space model with augmented aerodynamic lag states (using the Wagner function approximation of Sears) [34]. Analyses conducted by Tang et al. [26,27] used unsteady air loads in the time domain based on Peters' finite state model with augmented aerodynamic lag states (reduced-order eigenmodes) [37,38].

Calculations of the nonlinear responses with free-play effects have been made using both the describing function method and direct time integration of the equations of motion in Apex. Results from both linear and nonlinear stability analyses presented here were obtained using frequency-domain (k-value-dependent) two-dimensional incompressible unsteady air loads of Theodorsen [36]. Results from the nonlinear time-history response analyses presented here were obtained using time-domain unsteady aerodynamics computed by Apex with a rational function approximation (RFA) transformation of the frequency-dependent unsteady Theodorsen-type air loads.

Downloaded by UNIVERSITY OF WASHINGTON on August 12, 2019 | http://arc.aiaa.org | DOI: 10.2514/1.31901

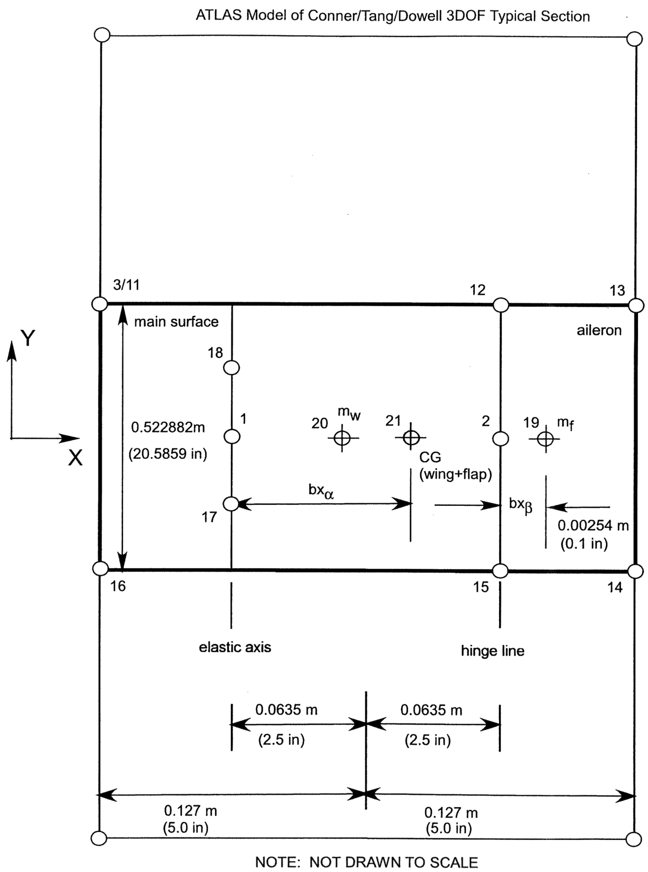

Fig. 4 ATLAS model of 3 DOF typical section.

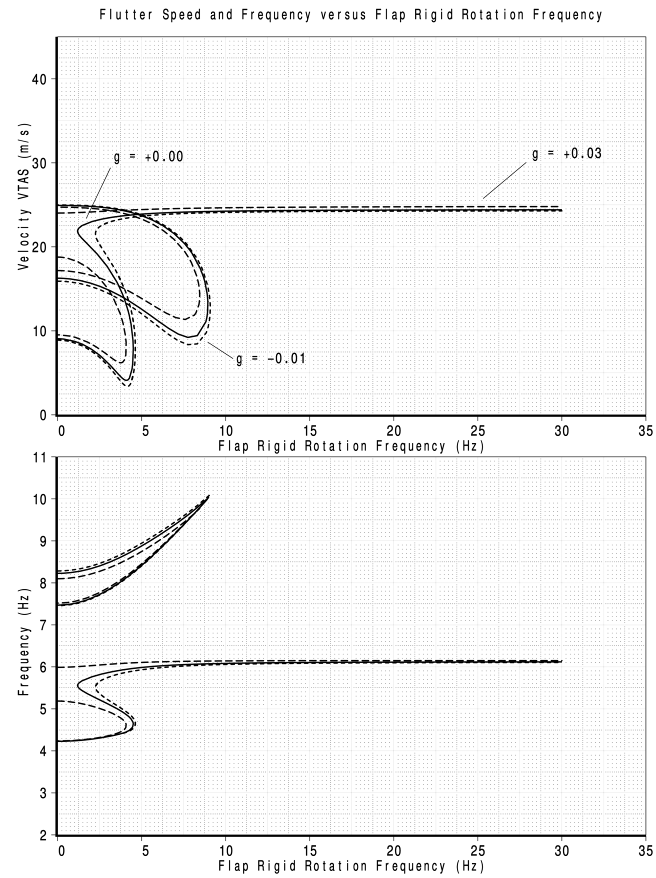

Fig. 5 Flutter speed and frequency vs flap rigid-rotation frequency.

These time-history integration analyses have replicated the four distinct regions of oscillatory behavior described by Conner [33], Conner et al. [25], and Tang et al. [26,27].

B. Linear System Stability Analysis Results

Figure 5 presents plots of flutter speed and frequency vs flap rigid rotation frequency ω_β for the 3 DOF typical-section ATLAS model (linear system) with flap frequencies varying from 0.0 to 30.0 Hz. Note that the nominal value of the flap rigid rotation frequency is $\omega_{\beta_{\mathrm{nom}}} = 17.39$ Hz, and that the flutter speed changes only slightly for $\omega_\beta > 17.39$ Hz. Figure 5 presents data at 3 growth rate levels, $g = 2\sigma/\omega = (-0.01, +0.0001, +0.03)$, where σ and ω are the real and imaginary parts of the flutter eigenvalue, respectively. Growth rate is defined as the negative of the decay rate. Note that the curve for a growth rate $g = +0.0001$ is identified on the plot as $g = +0.00$. These flutter solutions were obtained using the Apex program's continuation method p–k solver to track the roots of each system mode for the h, α, and β coordinates at specified growth rate levels. Note also that a specific flutter speed can occur at multiple values of the flap rotation frequency.

Results presented in this section were obtained using a viscous damping matrix B_S for the nominal flap rotation frequency as described by Conner et al. [25] because the effect on flutter speed was minimal due to changes in B_S for $\omega_\beta < \omega_{\beta\mathrm{nom}}$.

In Fig. 5, there are three flutter speeds of particular interest besides the flutter speed U_F for the nominal flap rotation frequency. One is $U_{F0} \approxeq 9.52$ m/s, which occurs at $\omega_\beta = 0$ Hz for an unconstrained (free) control surface. Another is $U_{F\min} \approxeq 4.12$ m/s, which occurs at $\omega_\beta \approxeq 4.0$ Hz and is the minimum flutter speed for all ω_β. At a flap rotation frequency $\omega_\beta \approxeq 8.0$ Hz, a secondary (local) minimum flutter speed $U_{F\min 2} \approxeq 9.77$ m/s occurs. At a flap rotational frequency $\omega_\beta \approxeq 4.5$–$5.0$ Hz, the flutter frequency jumps from a low frequency (near the plunge natural frequency) to a higher frequency (near the pitch natural frequency). At a flap rotational frequency $\omega_\beta \approxeq 9.0$ Hz, the flutter frequency drops to a lower frequency ($\omega_F \approxeq 6.0$ Hz). For the ATLAS model of the 3 DOF typical section with a nominal flap rotation frequency $\omega_{\beta\mathrm{nom}} = 17.39$ Hz, the flutter speed is $U_F = 24.36$ m/s.

C. Nonlinear Stability Analysis Results

In this section results are presented from nonlinear stability analyses for the 3 DOF typical-section ATLAS model with control surface free play that have been conducted with the describing function module in Apex. These nonlinear analyses have used frequency-domain (k-value-dependent) two-dimensional incompressible unsteady air loads computed by ATLAS. Also presented in this section are results from nonlinear time-response analyses that have used time-domain unsteady air loads computed by Apex with a RFA transformation of the frequency-dependent unsteady air loads from ATLAS. The time-history response predictions are compared with nonlinear response amplitudes determined by the describing function method. All results shown here have used a specific free-play value $\delta_{\mathrm{fp}} = \pm 0.037$ rad (± 2.12 deg) for the control surface rigid rotation degree of freedom β. All responses scale in proportion to the free play. All response amplitudes have been made nondimensional and have been normalized with respect to the free play δ_{fp}.

Results presented in this section were obtained using a viscous damping matrix B_S for the nominal flap rotation frequency as described by Conner et al. [25] because the effect on flutter speed from changes in B_S for frequencies in the range $0 \leq \omega_\beta < \omega_{\beta\mathrm{nom}}$ had been found to be minimal.

Figure 6 presents a plot showing the nonlinear response amplitude and frequency of the flap rigid rotation coordinate β vs flow speed for three growth-rate levels $g = (-0.01, +0.0001, \text{and} + 0.03)$ for a free play $\delta_{\mathrm{fp}} = 0.037$ rad. Note that the curve for a growth rate $g = +0.0001$ is identified on the plot as $g = +0.00$. A growth rate $g < 0$ indicates stability of the linear system; $g > 0$ indicates instability.

Downloaded by UNIVERSITY OF WASHINGTON on August 12, 2019 | http://arc.aiaa.org | DOI: 10.2514/1.31901

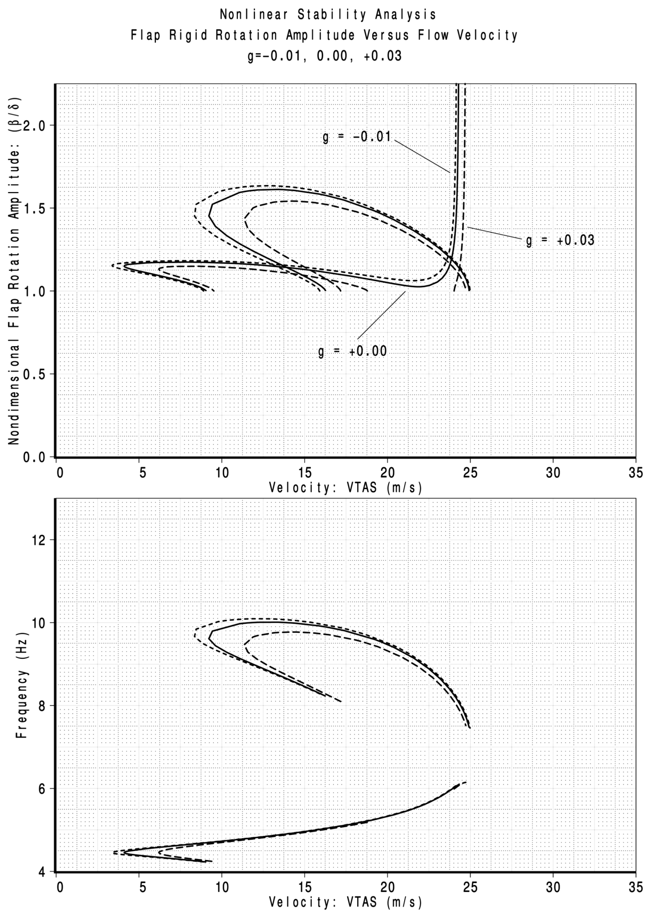

Fig. 6 Nondimensional flap rotation vs flow speed; $g = (-0.01, +0.0001, +0.03)$.

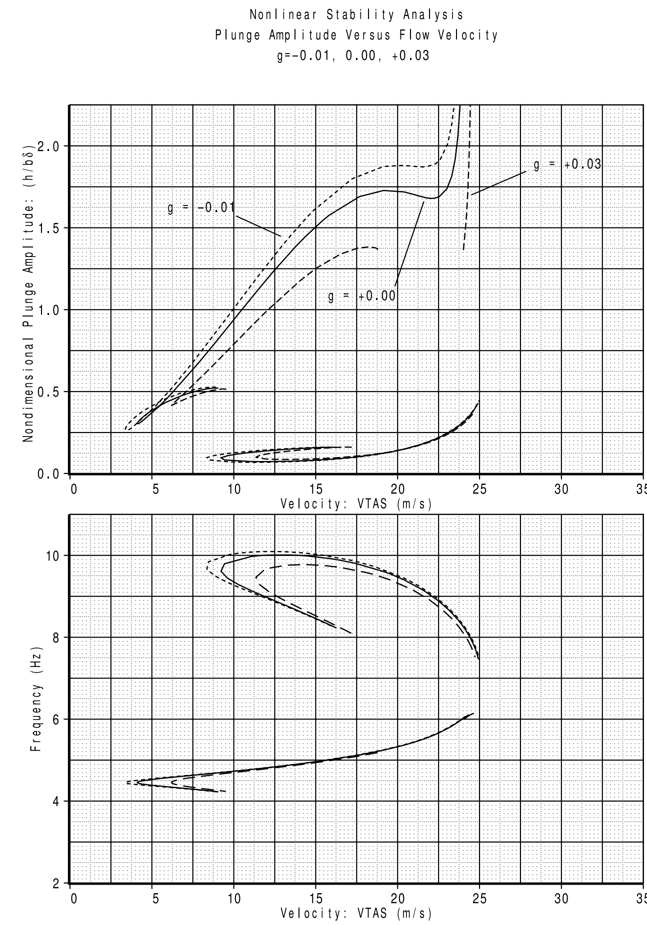

Fig. 7 Nondimensional section plunge vs flow speed; $g = (-0.01, +0.0001, +0.03)$.

Stability of the periodic solution ($\sigma = 0$) for the nonlinear system is determined by the change in amplitude A when the real part of the eigenvalue $\sigma = 0$. If, for an increase in the amplitude A from its value A_{LC} for the periodic solution (i.e., at the limit cycle), the function $\sigma(A)$ changes sign from positive to negative, the periodic solution is stable, and vice versa. Hence, stability of the periodic solution is determined by the sign of the ratio $\Delta\sigma/\Delta A$ rather than merely the sign of $\sigma(A)$. For a stable limit cycle to exist, $\{\frac{\partial\sigma}{\partial A}\}_{A=A_{\mathrm{LC}}} < 0$. For an unstable limit cycle to exist, $\{\frac{\partial\sigma}{\partial A}\}_{A=A_{\mathrm{LC}}} > 0$.

This limit cycle stability criteria can be evaluated directly from the nonlinear response plots shown in Fig. 6. Consider the nonlinear response curves (giving limit cycle amplitude vs flow speed) for a growth rate $g = +0.00$. If the response curve for a lower growth rate (e.g., $g = -0.01$) lies above the reference curve ($g = +0.00$), and the response curve for a higher growth rate ($g = +0.03$) lies below the reference curve, then the limit cycle is stable. If the positions of the lower and higher growth curves relative to the reference curve are reversed, the limit cycle is unstable. Of course, evaluation of stability requires that growth rates very close to the reference growth rate be used. The levels $g = -0.01$ and $g = +0.03$ have been used here to make visualization easier.

Consider the response curves for the nominal flutter crossing solutions $g = +0.0001$ in Fig. 6. As the flow speed increases from zero, the system is completely stable. Any initial displacement to the system will produce oscillatory responses that decay to 0 amplitude and the system is stable, reaching a static equilibrium. At a flow speed $U \approxeq 4.12$ m/s, for sufficiently large disturbances, the system experiences a jump to a stable limit cycle (the upper branch of the curve for $g = +0.0001$). For disturbances of amplitude greater than the lower branch of the solid curve, responses will grow to the upper curve (for disturbances of amplitude greater than the upper branch, responses will decay to the upper curve) and then oscillate at the frequency ($\omega \approxeq 4.5$ Hz) determined from the corresponding branch of the $g = +0.0001$ curve shown in Fig. 6, that is, a stable limit cycle oscillation (LCO) exists. For disturbances of amplitude less than the lower branch of the solid curve (the lower branch represents an unstable LCO), responses will decay to 0 amplitude and the system is locally stable. For flow speeds $U \gtrapprox 9.00$ m/s, a stable LCO will occur because the lower unstable LCO branch exists only for the range $4.12 \lessapprox U \lessapprox 9.00$ m/s.

In Fig. 6, as the flow speed continues to increase for $U \gtrapprox 9.26$ m/s another pair of unstable and stable LCO branches are encountered. For disturbance amplitudes greater than the lower branch of the upper solid curve, responses will grow to the new stable LCO branch (uppermost curve) and then oscillate at the higher frequency ($\omega \approxeq 9.5$–10.0 Hz) for the corresponding branch of the $g = +0.0001$ curve. This stable LCO branch is followed as the flow speed continues to increase until $U \approxeq 24.00$ m/s when there is a jump back down to the lower frequency LCO branch ($\omega \approxeq 6.0$ Hz). The LCO amplitude then grows asymptotically to infinity as the flow speed U increases to the flutter speed U_F of the nominal system ($\omega_\beta = \omega_{\beta_{\mathrm{nom}}}$). For disturbance amplitudes less than the lower branch of the upper solid curve, responses will decay to the amplitude of the lower stable LCO curve in the flow speed range $9.26 \lessapprox U \lessapprox 13.89$ m/s.

Figure 7 presents a plot showing the nonlinear response amplitude of the plunge coordinate h vs flow speed for three growth-rate levels (-0.01, $+0.0001$, and $+0.03$) for a free play $\delta_{\mathrm{fp}} = 0.037$ rad. The character of the nonlinear response for the plunge coordinate h is seen to be quite different than that for the flap coordinate β shown in Fig. 6. No LCO exists for flow speeds $0 < U \lessapprox 4.12$ m/s at which point a low-frequency LCO ($\omega \approxeq 4.5$ Hz) appears. The LCO amplitude of the plunge coordinate in this low-frequency mode increases asymptotically to infinity with increasing flow speed as $U \to U_F$. However, unlike the situation in Fig. 6 for the flap rotation

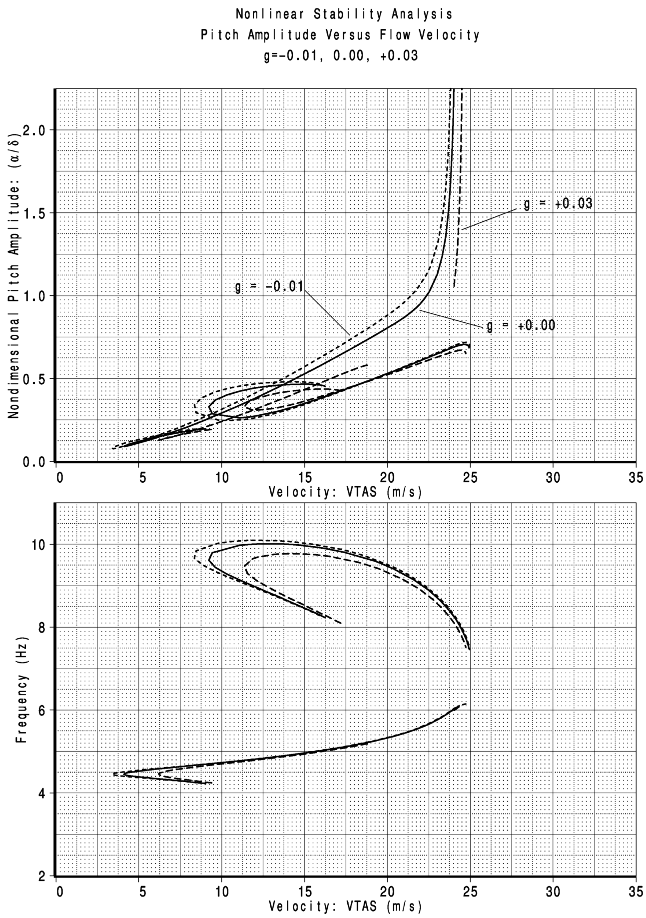

Fig. 8 Nondimensional section pitch vs flow speed; $g = (-0.01, +0.0001, +0.03)$.

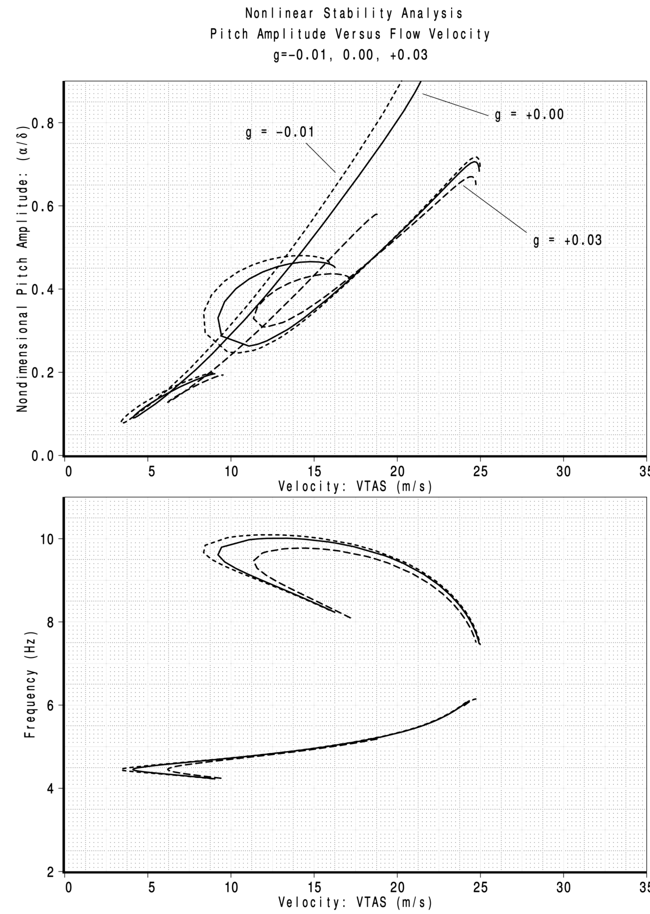

Fig. 9 Nondimensional section pitch vs flow speed (expanded scale); $g = (-0.01, +0.0001, +0.03)$.

coordinate β, there is now a lower amplitude LCO occuring at a higher frequency ($\omega \approxeq 9.5$–10.0 Hz) for flow speeds $U \gtrapprox 9.26$ m/s.

Figure 8 presents a plot showing the nonlinear response amplitude of the pitch coordinate α vs flow speed for three growth-rate levels (-0.01, $+0.0001$, and $+0.03$) for a free play $\delta_{\mathrm{fp}} = 0.037$ rad. Figure 9 presents the same plot shown in Fig. 8 but with an expanded scale for the response amplitude of the pitch coordinate α.

The character of the nonlinear response for the pitch coordinate α shown in Figs. 8 and 9 is seen to exhibit aspects of the responses for both the flap rotation coordinate β shown in Fig. 6 and the plunge coordinate h shown in Fig. 7. No LCO exists for flow speeds $0 < U \lessapprox 4.12$ m/s at which point a low frequency ($\omega \approxeq 4.5$ Hz) LCO appears with a behavior similar to that of the plunge coordinate. The LCO amplitude of the pitch coordinate in this low-frequency mode increases asymptotically to infinity with increasing flow speed as $U \rightarrow U_F$. Somewhat like the situation in Fig. 6 for the flap rotation coordinate β, there is now a higher amplitude LCO occuring at a higher frequency ($\omega \approxeq 9.5$–10.0 Hz) for flow speeds $U \gtrapprox 9.26$ m/s. Application of the limit cycle stability criteria given in Chapter 2 identifies the upper branch of this low-frequency mode as a stable LCO branch for flow speeds $9.26 < U \lessapprox 16.21$ m/s. The lower branch of the high-frequency mode's response curve represents an unstable LCO for flow speeds $9.26 < U \lessapprox 18.01$ m/s and a stable LCO for flow speeds $18.01 < U \lessapprox 24.00$ m/s.

D. Comparison of Predicted Nonlinear Responses and Test Data

Time-history responses for the 3 DOF typical-section model with control surface free play have been computed by numerical integration using a Runge–Kutta algorithm and a time step $\Delta t = 5.0 \times 10^{-5}$ s with the Apex program. These calculations have used the nonlinear model having symmetric free play about the flap hinge line discussed in the preceding paragraphs with the nominal parameter values given in the Appendix for flow speeds $0 < U < U_F = 24.36$ m/s and control surface free play $\delta_{\mathrm{fp}} = 0.037$ rad. Time-domain unsteady air loads computed by Apex with a RFA transformation of the frequency-dependent unsteady air loads from ATLAS have been used. Five aerodynamic lag states ($\beta_{\mathrm{lag}} = 0.0005$, 0.005, 0.1, 0.5, 0.9) have been used. Determination of the final aerodynamic lag state conditions was made by varying both the number of lag states and the β_{lag} values until a close match was obtained between the flutter speed vs growth rate plot from the RFA flutter solution and that from the flutter solution using the frequency-domain air loads (k-value-dependent) from ATLAS for each aeroelastic mode.

Figures 10–13 present comparisons of test data from Tang et al. [27] with nonlinear response amplitudes of the flap rotation, plunge, and pitch coordinates (β, h, α) vs flow speed predicted by both describing function method and time-history integration solutions for a free play $\delta_{\mathrm{fp}} = 0.037$ rad.

Figure 10 presents a comparison of test data with nonlinear response amplitudes of the flap rigid rotation coordinate β vs flow speed predicted by the describing function method and by time-history integration for a free play $\delta_{\mathrm{fp}} = 0.037$ rad. Response amplitudes from the describing function analyses are given for three growth-rate levels (-0.01, $+0.0001$, and $+0.03$). Consider the response curves for the nominal flutter crossing solutions $g = +0.0001$ in Fig. 10. As the flow speed increases from zero, the system is completely stable. Any initial displacement to the system will produce oscillatory responses that decay to 0 amplitude, and the system is stable, reaching a static equilibrium. At a flow speed $U \approxeq 4.12$ m/s (4.63 m/s for time-history response solution and 5.40 m/s for test data), for sufficiently large disturbances, the system experiences a jump to a stable limit cycle (the upper branch of the curve for $g = +0.0001$). For disturbances of amplitude greater than the lower branch of the solid curve, responses will grow to the upper curve and then oscillate at the frequency ($\omega \approxeq 4.5$ Hz) determined from the corresponding branch of the $g = +0.0001$ curve shown in

Downloaded by UNIVERSITY OF WASHINGTON on August 12, 2019 | http://arc.aiaa.org | DOI: 10.2514/1.31901

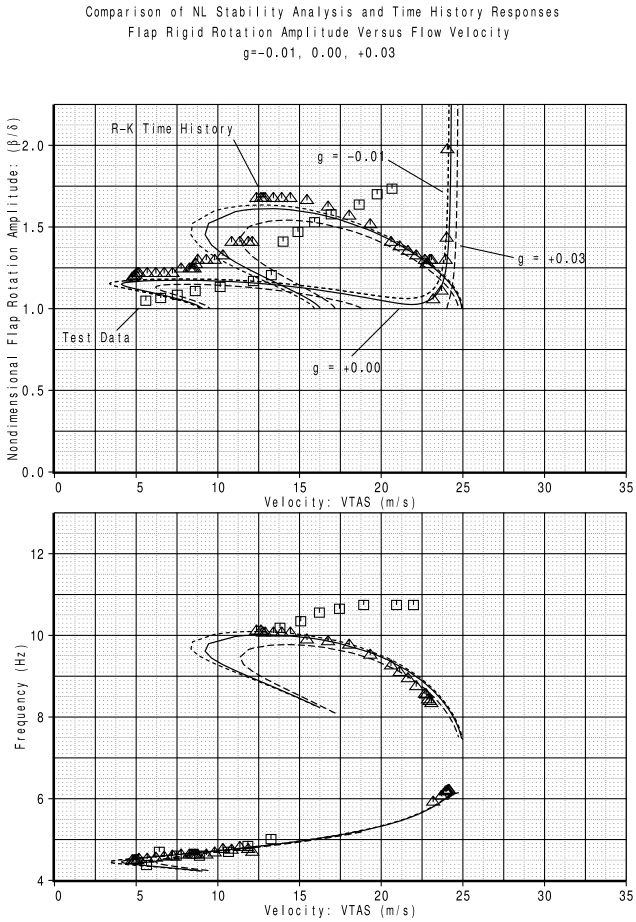

Fig. 10 Nondimensional flap rotation vs flow velocity, comparison with test data; free play $\delta_{\mathrm{fp}} = 0.037$ rad; $g = (-0.01, +0.0001, +0.03)$.

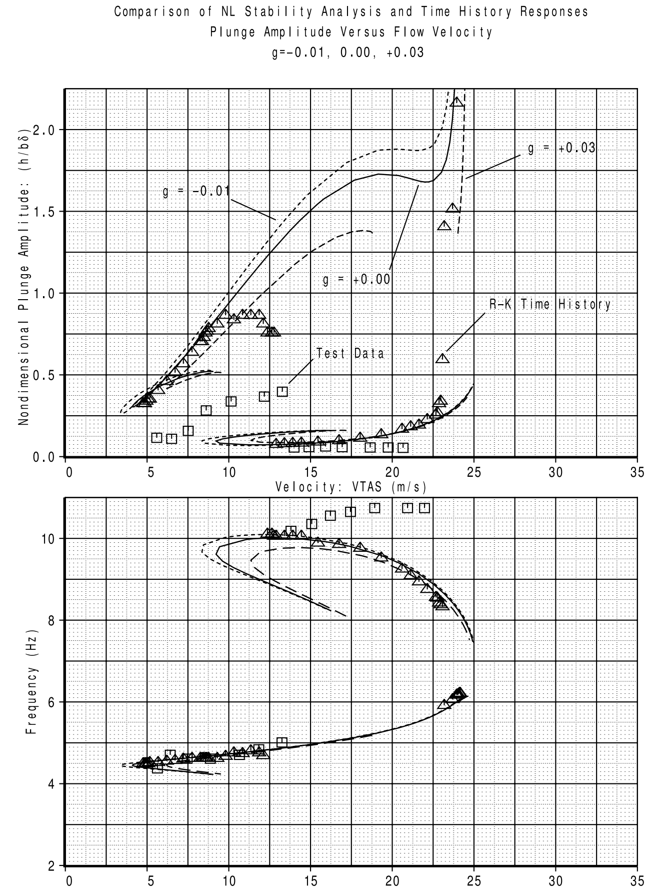

Fig. 11 Nondimensional section plunge vs flow velocity, comparison with test data; free play $\delta_{\mathrm{fp}} = 0.037$ rad; $g = (-0.01, +0.0001, +0.03)$.

Fig. 6, that is, a stable limit cycle oscillation (LCO). For disturbances of amplitude less than the lower branch of the solid curve, responses will decay to 0 amplitude and the system is locally stable. Note that for flow speeds $U \gtrapprox 9.00$ m/s a stable LCO will occur because the lower unstable LCO branch exists only for the range $4.12 \lessapprox U \lessapprox 9.00$ m/s.

In Fig. 10, as the flow speed continues to increase for $U \gtrapprox 9.26$ m/s, another pair of unstable and stable LCO branches are encountered. For disturbance amplitudes greater than the lower branch of the upper solid curve, responses will grow to the new stable LCO branch (uppermost curve) and then oscillate at the higher frequency ($\omega \approxeq 9.5$–10.0 Hz) for the corresponding branch of the $g = +0.0001$ curve. This stable LCO branch is followed as the flow speed continues to increase until $U \approxeq 23.00$ m/s when there is a jump back down to the lower frequency LCO branch ($\omega \approxeq 6.0$ Hz). The LCO amplitude then grows asymptotically to infinity as the flow speed U increases to the flutter speed U_F of the nominal system ($\omega_\beta = \omega_{\beta_{\mathrm{nom}}}$). For disturbance amplitudes less than the lower branch of the upper solid curve, responses will decay to the amplitude of the lower stable LCO curve in the flow speed range $9.26 \lessapprox U \lessapprox 13.89$ m/s.

Comparison of the time-history response and describing function results for the flap rotation β, shown in Fig. 10, is extremely good for flow speeds in the ranges $4.12 \lessapprox U \lessapprox 9.00$ m/s and $12.35 \lessapprox U \lessapprox 24.36$ m/s. In particular, the comparison is excellent for speeds $U \gtrapprox 20.58$ m/s including capture of the change in mode and drop in amplitude that occurs at $U \approxeq 23.00$ m/s. In the region $8.75 \lessapprox U \lessapprox 12.09$ m/s, the comparisons between time-history response and describing function results are only fair with time-history amplitudes lying approximately midway between the lower and upper LCO branches predicted by the describing function method. This range of flow speeds is the transition region, which consists of a more complex periodic low-frequency limit cycle that exhibits several types of nonlinear behavior including quasiperiodicity. Test data (Tang et al. [27]) is also shown in Fig. 10 for flow speeds $U \lessapprox 20.58$ m/s. Test data and analytically predicted amplitudes compare fairly well for speeds $U \lessapprox 14.15$ m/s; agreement is less good for speeds $U \gtrapprox 14.15$ m/s. Experimental and analytical frequencies compare very well for speeds $U \lessapprox 14.15$ m/s; agreement is only fair in the speed range $15.43 \lessapprox U \lessapprox 21.86$ m/s.

Figure 11 presents a comparison of test data with nonlinear response amplitudes of the section plunge coordinate h vs flow speed predicted by the describing function method and by time-history integration for a free play $\delta_{\mathrm{fp}} = 0.037$ rad. Response amplitudes from the describing function analyses are given for three growth-rate levels (-0.01, $+0.0001$, and $+0.03$).

Comparison of the time-history response and describing function results for the section plunge coordinate h, shown in Fig. 11, is extremely good for flow speeds in the range $4.12 \lessapprox U \lessapprox 9.77$ m/s and $12.86 \lessapprox U \lessapprox 23.15$ m/s. In particular, the comparison is excellent for speeds $U \lessapprox 9.00$ m/s and in the speed range $12.86 \lessapprox U \lessapprox 18.01$ m/s including capture of the change in mode and drop in amplitude that occurs at $U \approx 12.86$ m/s. In the region $10.29 \lessapprox U \lessapprox 12.60$ m/s, the comparisons between time-history response and describing function results are only fair with time-history amplitudes lying approximately midway between the lower and upper LCO branches predicted by the describing function method. This range of flow speeds is the transition region, which consists of a more complex periodic low-frequency limit cycle that exhibits several types of nonlinear behavior including quasiperiodicity.

Test data (Tang et al. [27]) are also shown in Fig. 11 for flow speeds $U \lessapprox 20.58$ m/s. Comparison between test data and analytically predicted plunge amplitudes is fair for speeds $U \lessapprox 12.86$ m/s; agreement is excellent for speeds $12.86 \lessapprox U \lessapprox 18.01$ m/s and good for speeds $18.01 \lessapprox U \lessapprox 20.58$ m/s.

Downloaded by UNIVERSITY OF WASHINGTON on August 12, 2019 | http://arc.aiaa.org | DOI: 10.2514/1.31901

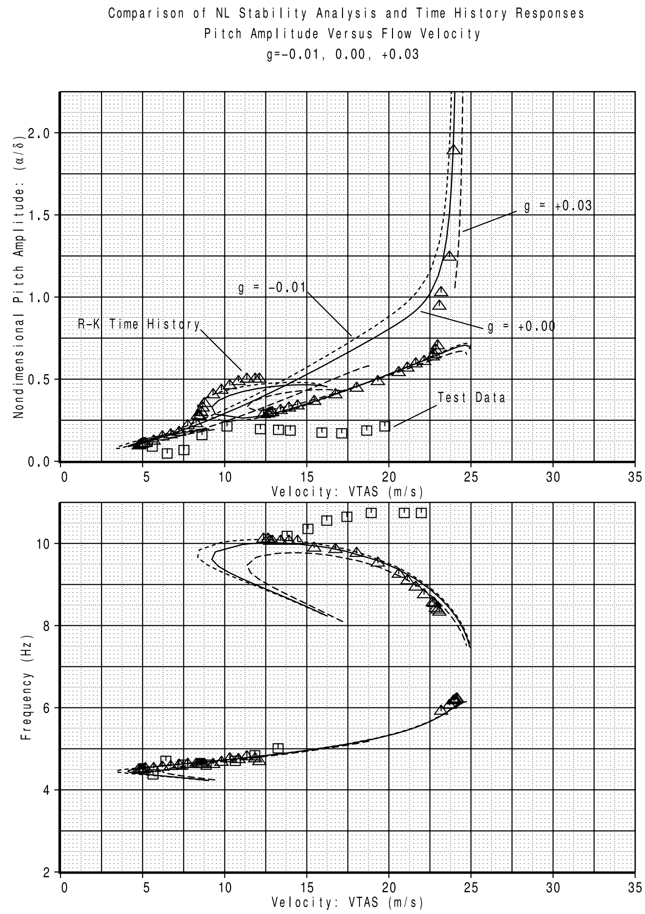

Fig. 12 Nondimensional section pitch vs flow velocity, comparison with test data; free play $\delta_{fp} = 0.037$ rad; $g = (-0.01, +0.0001, +0.03)$.

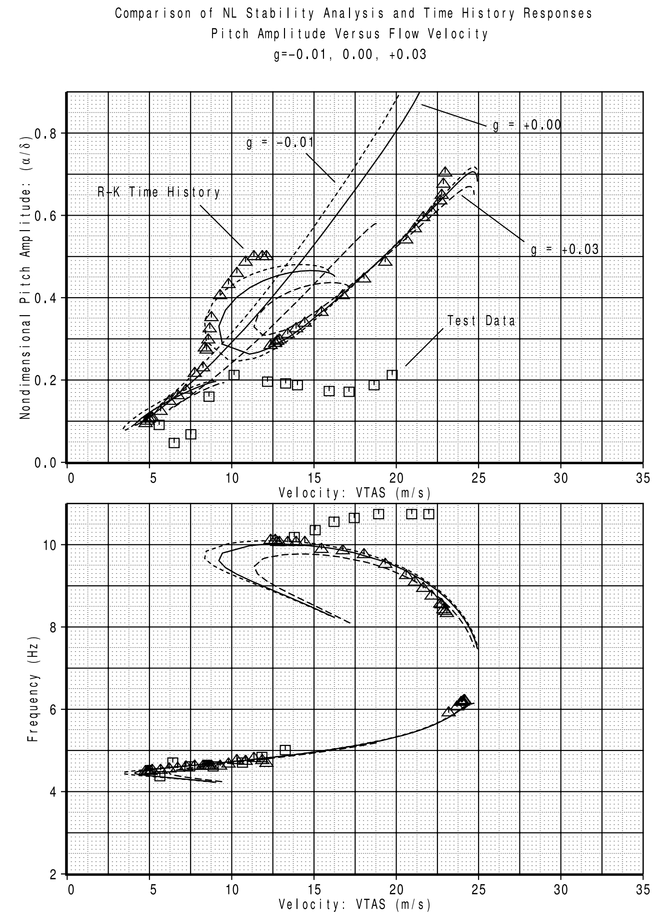

Fig. 13 Nondimensional section pitch vs flow velocity, comparison with test data (expanded scale); free play $\delta_{fp} = 0.037$ rad; $g = (-0.01, +0.0001, +0.03)$.

Experimental and analytical frequencies compare very well for speeds $U \lessapprox 14.15$ m/s; agreement is only fair in the speed range $15.43 \lessapprox U \lessapprox 21.86$ m/s.

Figure 12 presents a comparison of test data with nonlinear response amplitudes of the section pitch coordinate α vs flow speed predicted by the describing function method and by time-history integration for a free play $\delta_{fp} = 0.037$ rad. Response amplitudes from the describing function analyses are given for three growth-rate levels (-0.01, $+0.0001$, and $+0.03$). Figure 13 presents the same plot shown in Fig. 12 but with an expanded scale for the response amplitude of the section pitch coordinate α.

Comparison of the time-history response and describing function results for the section pitch coordinate α, shown in Figs. 12 and 13, is very good for all flow speeds in the range $4.12 \lessapprox U \lessapprox 23.15$ m/s, including capture of the change in amplitude and frequency that occur at $U \approx 12.86$ m/s and at $U \approx 23.15$ m/s. In the transition region, $8.75 \lessapprox U \lessapprox 12.09$ m/s, the comparisons between time-history response and describing function results for the pitch coordinate α are seen to be much better than for the flap rotation coordinate β shown in Fig. 10.

Test data (Tang et al. [27]) are also shown in Figs. 12 and 13 for flow speeds $U \lessapprox 20.58$ m/s. Test data and analytically-predicted pitch amplitudes compare fairly well for speeds $U \lessapprox 12.86$ m/s; agreement is less good for speeds $U \gtrapprox 14.15$ m/s. Experimental and analytical frequencies compare very well for speeds $U \lessapprox 14.15$ m/s; agreement is only fair in the speed range $15.43 \lessapprox U \lessapprox 21.86$ m/s.

Figures 5 and 6 of Tang et al. [27] present comparisons of test data with describing function and time-integration solutions for the flap rotation response vs flow speed and for the plunge and pitch responses versus flow speed, respectively. Note that the flow speed has been normalized to $U_{F0} = 8.6$ m/s for $K_\beta = 0$ in these plots.

A comparison of the analytical results shown in Figs. 5 and 6 of Tang et al. [27] and the results from ATLAS/Apex analyses given in Figs. 10–13 shows that the agreement between the describing function and time-history integration solutions is generally better for the ATLAS/Apex analyses than was obtained by Tang et al. (comparing only results from the two types of analytical solutions, not with the test data). Possible reasons for the improved comparison over that obtained by Tang et al. are the use of the locally parameterized continuation method to track all flutter modes and the different number of aerodynamic states used in the RFA transformed air loads (five lag states for the ATLAS/Apex analyses vs four aerodynamic eigenmode states used by Tang et al. with Peter's finite state model). Tang et al. results showed that the use of more than four aerodynamic eigenmodes caused only a slight change in the flutter speed. Otherwise, the primary difference in the models is the use of frequency-domain Theodorsen unsteady aerodynamics for the ATLAS/Apex describing function analyses and use of Peter's finite state model by Tang et al. Comparisons of test data shown in Figs. 5 and 6 of Tang et al. [27] and analytical results are reasonable for both Tang et al. and the ATLAS/Apex solutions (good to excellent in some speed ranges and fair-to-poor in others). During the Duke University wind-tunnel testing [25], the coupled natural frequencies (pitch, control surface rotation, and plunge) of the model were measured before and after the tests were conducted. Decreases in these coupled frequencies of 12.3, 2.05, and 2.94% were noted for the pitch, control surface rotation, and plunge freedoms, respectively. The small-diameter steel-wire leaf spring, which provided torsional stiffness for the pitching motion, was considered particularly vulnerable to the forces generated near flutter or imposed by the physical stops used to limit the range of motion. The decreases in coupled frequencies were considered most likely to be caused by changes in the torsional stiffness for the pitch degree of freedom, which could explain some of the discrepancy between numerical and experimental flutter boundaries [25].

Downloaded by UNIVERSITY OF WASHINGTON on August 12, 2019 | http://arc.aiaa.org | DOI: 10.2514/1.31901

Downloaded by UNIVERSITY OF WASHINGTON on August 12, 2019 | http://arc.aiaa.org | DOI: 10.2514/1.31901

IV. Conclusions

A methodology for the nonlinear stability analysis of control surface flutter, including free-play effects, has been developed that uses the describing function technique to predict response amplitudes and a locally-parameterized continuation method to track all flutter modes. Both stable and unstable limit cycles have been identified and limit cycle stability has been assessed by examining the change in growth rate due to amplitude perturbations at a given velocity.

Results were presented from nonlinear flutter analyses conducted on a three-degree-of-freedom typical-section airfoil with free play about the control surface hinge line using describing function and direct time-integration techniques. Limit-cycle amplitudes predicted by the describing function method, with frequency-domain unsteady aerodynamics, were shown to compare very well with the magnitudes of time-history responses obtained by direct integration of the nonlinear equations of motion, using rational function approximation time-domain aerodynamics. Predicted responses from the describing function and time-integration analyses were also shown to compare favorably with both analytical and experimental results documented in the open literature.

Table A1 Dependent variables

Quantity	Description
α	Pitch rotation
β	Control surface rotation
h	Plunge displacement (nondimensional with respect to b)
$\dot{\alpha}$	Pitch rotational velocity
$\dot{\beta}$	Control surface rotational velocity
$\dot{h}$	Plunge velocity
$\mathbf{x}$	Vector of generalized coordinates (α, β, h)
$\mathbf{x_i}$	Augmented state variable for β_i with RFA aerodynamics
$s\mathbf{x_i}$	Augmented state velocity, $s\mathbf{x_i} = s\mathbf{x} - v_t \beta_i \mathbf{x_i}$
v_t	True airspeed
β_i	ith aerodynamic lag value

Appendix A: 3 DOF Typical-Section Flutter Model Parameters

Table A3 Parameter values

Parameter	Numerical values
b	0.127 m
a	-0.5
c	$+0.5$
K_α	$1486.0\ \mathrm{N \cdot m/(kg \cdot m^2)} \sim 1/\mathrm{s}^2$
K_β	$155.0\ \mathrm{N \cdot m/(kg \cdot m^2)} \sim 1/\mathrm{s}^2$
K_h	1809.0 N/kg
m_{wing}	0.62868 kg
m_{flap}	0.18597 kg
m_{ref}	1.558 kg/m
m_{sup}	(0.47485×2) kg
r_α	0.7328
r_β	0.1141
x_α	0.4347
x_β	0.0200
S_α	$0.08587\ \mathrm{kg \cdot m}$
S_β	$0.00395\ \mathrm{kg \cdot m}$
ζ_α	0.01626
ζ_β	0.01150
ζ_h	0.01130
κ	0.03991

Table A2 Parameter definitions

Parameter	Description and units
b	Semichord
a	Elastic axis position with respect to b
c	Hinge line position with respect to b
m_{wing}	Wing mass
m_{flap}	Flap (aileron) mass
m_{ref}	Reference mass (wing mass + flap mass per unit span)
m_{sup}	Support mass (per unit span)
m_{tot}	Total mass in plunge coordinate $= m_{\mathrm{ref}} + m_{\mathrm{sup}}$ (per unit span)
F_{fp}	Restoring moment due to free play
r_α^2	$I_\alpha/(m_{\mathrm{ref}} b^2)$
r_β^2	$I_\beta/(m_{\mathrm{ref}} b^2)$
x_α	$S_\alpha/(m_{\mathrm{ref}} b) = m_{\mathrm{ref}} x_{\mathrm{cg}}/(m_{\mathrm{ref}} b)$
x_β	$S_\beta/(m_{\mathrm{ref}} b) = m_{\mathrm{flap}} x_{\mathrm{cg\ flap}}/(m_{\mathrm{ref}} b)$
I_α	Rotational inertia of wing and flap (aileron) about the elastic axis
I_β	Rotational inertia of flap (aileron) about the hinge line
K_α	$\bar{K}_\alpha/(m_{\mathrm{ref}} b^2) = r_\alpha^2 \bar{\omega}_\alpha^2$
K_β	$\bar{K}_\beta/(m_{\mathrm{ref}} b^2) = r_\beta^2 \bar{\omega}_\beta^2$
K_h	$\bar{K}_h/m_{\mathrm{ref}} = \bar{\omega}_h^2$
$\bar{K}_\alpha$	Torsional stiffness per unit length of wing about a
$\bar{K}_\beta$	Torsional stiffness per unit length of aileron about c
$\bar{K}_h$	Stiffness of wing in deflection per unit length
S_α	Static moment of wing-aileron (per unit span) about a
S_β	Static moment of aileron (per unit span) about c
ζ_α	Pitch modal damping ratio
ζ_β	Flap modal damping ratio
ζ_h	Plunge modal damping ratio
ω_α	Pitch coupled natural frequency (Hz)
ω_β	Flap coupled natural frequency (Hz)
ω_h	Plunge coupled natural frequency (Hz)
$\bar{\omega}_\alpha$	Wing torsional uncoupled natural frequency (Hz) about a
$\bar{\omega}_\beta$	Flap torsional uncoupled natural frequency (Hz) about c
$\bar{\omega}_h$	Wing plunge uncoupled natural frequency (Hz)
κ	$\pi \rho b^2/m_{\mathrm{ref}} =$ mass ratio

References

[1] Dowell, E. H., and Tang, D., "Nonlinear Aeroelasticity and Unsteady Aerodynamics," *AIAA Journal*, Vol. 40, No. 9, 2002, pp. 1697–1707.

[2] Dowell, E., Edwards, J., and Strganac, T., "Nonlinear Aeroelasticity," *Journal of Aircraft*, Vol. 40, No. 5, 2003, pp. 857–874.

[3] Schuster, D. M., Liu, D. D., and Huttsell, L. J., "Computational Aeroelasticity: Success, Progress, Challenge," *Journal of Aircraft*, Vol. 40, No. 5, 2003, pp. 843–856.

[4] Yurkovich, R., "Status of Unsteady Aerodynamic Prediction for Flutter of High-Performance Aircraft," *Journal of Aircraft*, Vol. 40, No. 5, 2003, pp. 832–842.

[5] Krylov, N. M., and Bogoliubov, N. N., *Introduction to Nonlinear Mechanics*, Translated by S. Lefschetz, Princeton Univ. Press, Princeton, NJ, 1947.

[6] Šiljak, D. D., *Nonlinear Systems*, Wiley, New York, 1969, pp. 107–151.

[7] Popov, E. P., "On the Use of the Harmonic Linearization Method in Automatic Control Theory," NACA TM 1406, Jan. 1957.

[8] Woolston, D. S., Runyan, H. L., and Andrews, R. E., "An Investigation of Effects of Certain Types of Structural Nonlinearities on Wing and Control Surface Flutter," *Journal of the Aeronautical Sciences*, Vol. 24, No. 1, Jan. 1957, pp. 57–63.

[9] Shen, S. F., "An Approximate Analysis of Nonlinear Flutter Problems," *Journal of the Aerospace Sciences*, Vol. 25, No. 1, Jan. 1959, pp. 25–32, 45.

[10] Breitbach, E. J., "Flutter Analysis of an Airplane with Multiple Structural Nonlinearities in the Control System," NASA Rept. TP-1620, 1980.

[11] Laurenson, R. M., and Trn, R. M., "Flutter Analysis of Missile Control Surfaces Containing Structural Nonlinearities," *AIAA Journal*, Vol. 18, No. 10, 1980, pp. 1245–1251.

[12] Laurenson, R. M., Hauenstein, J., Gubser, J. L., and Briley, R. P., "Effects of Structural Nonlinearities on Limit Cycle Response of Aerodynamic Surfaces," Proceedings of the 29th AIAA Structures, Structural Dynamics, and Materials Conference, AIAA, Paper 1986-0899, 1986, pp. 279–292.

[13] Lee, C. L., "An Iterative Procedure for Nonlinear Flutter Analysis," *AIAA Journal*, Vol. 24, No. 5, 1986, pp. 833–840.

[14] Yang, Z. C., and Zhao, L. C., "Analysis of Limit Cycle Flutter of an Airfoil in Incompressible Flow," *Journal of Sound and Vibration*, Vol. 123, No. 1, 1988, pp. 1–13.
doi:10.1016/S0022-460X(88)80073-7

[15] Lee, B. H. K., and Tron, A., "Effects of Structural Nonlinearities on Flutter Characteristics of the cf-18 Aircraft," *Journal of Aircraft*, Vol. 26, No. 8, 1989, pp. 781–786.
doi:10.2514/3.45839

[16] Price, S. J., Lee, B. H. K., and Alighanbari, H., "Postinstability Behavior of a Two-Dimensional Airfoil with Structural Nonlinearity," *Journal of Aircraft*, Vol. 31, No. 6, 1994, pp. 1395–1401.
doi:10.2514/3.46664

[17] Price, S. J., Alighanbari, H., and Lee, B. H. K., "The Aeroelastic Response of a Two-Dimensional Airfoil with Bilinear and Cubic Structural Nonlinearities," *Journal of Fluids and Structures*, Vol. 9, No. 2, 1995, pp. 175–193.
doi:10.1006/jfls.1995.1009

[18] Bogoliubov, N. N., and Mitropolskii, Y. A., *Asymptotic Methods in the Theory of Nonlinear Oscillations*, Hindustan Publishing Corp., New Delhi, India, 1961.

[19] Morrison, J. A., "Comparison of the Modified Method of Averaging and the Two Variable Expansion Procedure," *SIAM Review*, Vol. 8, No. 1, 1966, pp. 66–85.
doi:10.1137/1008006

[20] Cole, J. D., and Kevorkian, J., "Uniformly Valid Asymptotic Approximations for Certain Nonlinear Differential Equations," *Proceedings of the International Symposium on Nonlinear Differential Equations and Nonlinear Mechanics*, Academic Press, New York, 1963, pp. 113–120.

[21] Kevorkian, J., "The Two Variable Expansion Procedure for the Approximate Solution of Certain Nonlinear Differential Equations," *Space Mathematics, Part 3*, Lectures in Applied Mathematics, American Mathematical Society, Providence, RI, 1966.

[22] Nayfeh, A. H., "A Perturbation Method for Treating Nonlinear Oscillation Problems," *Journal of Mathematical Physics*, Vol. 44, No. 4, 1965, pp. 368–374.

[23] Nayfeh, A. H., *Perturbation Methods*, 1st ed., Wiley, New York, 1973.

[24] Nayfeh, A. H., and Mook, D. T., *Nonlinear Oscillations*, 1st ed., Wiley, New York, 1979.

[25] Conner, M. D., Tang, D. M., Dowell, E. H., and Virgin, L. N., "Nonlinear Behavior of a Typical Airfoil Section with Control Surface Freeplay: A Numerical and Experimental Study," *Journal of Fluids and Structures*, Vol. 11, No. 1, 1997, pp. 89–109.
doi:10.1006/jfls.1996.0068

[26] Tang, D., Conner, M. D., and Dowell, E. H., "Reduced-Order Aerodynamic Model and its Application to a Nonlinear Aeroelastic System," *Journal of Aircraft*, Vol. 35, No. 2, 1998, pp. 332–338.

[27] Tang, D., Dowell, E. H., and Virgin, L. N., "Limit Cycle Behavior of an Airfoil with a Control Surface," *Journal of Fluids and Structures*, Vol. 12, No. 7, 1998, pp. 839–858.
doi:10.1006/jfls.1998.0174.

[28] Trickey, S. T., Virgin, L. N., and Dowell, E. H., "The Stability of Limit-Cycle Oscillations in a Nonlinear Aeroelastic System," *Proceedings of the Royal Society of London, Series A: Mathematical and Physical Sciences*, Vol. 458, No. 2025, 2002, pp. 2203–2226.

[29] Roger, K. L., "Airplane Math Modeling Methods for Active Control Design," *NATO Advisory Group for Aerospace Research and Development Conference Proceedings*, AGARD CP-228, 1977, pp. 4:1–4:11.

[30] Rheinboldt, W. C., and Burkardt, J. V., "A Locally Parameterized Continuation Process," *ACM Transactions on Mathematical Software*, Vol. 9, No. 2, 1983, pp. 215–235.
doi:10.1145/357456.357460

[31] Rheinboldt, W. C., *Numerical Analysis of Parameterized Nonlinear Equations*, Wiley, New York, 1986.

[32] Meyer, E. E., "Application of a New Continuation Method to Flutter Equations," Proceedings of the 29th AIAA Structures, Structural Dynamics, and Materials Conference, AIAA Paper 1988-2350, 1988, pp. 1118–1123.

[33] Conner, M. D., "Nonlinear Aeroelasticity of an Airfoil Section with Control Surface Freeplay," Ph.D. Dissertation, Duke Univ., Durham, NC, 1996.

[34] Edwards, J., Ashley, H., and Breakwell, J., "Unsteady Aerodynamic Modeling for Arbitrary Motions," *AIAA Journal*, Vol. 17, No. 4, 1979, pp. 365–374.
doi:10.2514/3.7348

[35] Trickey, S. T., "Global and Local Dynamics of an Aeroelastic System with a Control Surface Freeplay Nonlinearity," Ph.D. Dissertation, Duke Univ., Durham, NC 2000.

[36] Theodorsen, T., "General Theory of Aerodynamic Instability and the Mechanism of Flutter," NACA, Rept. 496, 1935.

[37] Peters, D. A., and Johnson, M. J., "Finite-State Airloads for Deformable Airfoils on Fixed and Rotating Wings," *Proceedings of the Symposium on Aeroelasticity and Fluid/Structure Interaction*, American Society of Mechanical Engineers, Fairfield, NJ, Nov. 1994, pp. 1–28.

[38] Peters, D. A., and Cao, W. M., "Finite State Induced Flow Models Part 1: Two-Dimensional Thin Airfoil," *Journal of Aircraft*, Vol. 32, No. 2, 1995, pp. 313–322.
doi:10.2514/3.46718

Downloaded by UNIVERSITY OF WASHINGTON on August 12, 2019 | http://arc.aiaa.org | DOI: 10.2514/1.31901